

MINISTRY OF
INDUSTRY AND
TRADE

MINISTRY OF
EDUCATION AND
TRAINING

NATIONAL RESEARCH INSTITUTE
OF MECHANICAL ENGINEERING

NARIME

MAI TAT LỢI

RESEARCH ON MACHINING THE
EXTERNAL CYLINDRICAL SURFACE
USING ELECTRICAL DISCHARGE MACHINING (*EDM*)
WITH ULTRASONIC VIBRATION ASSISTANCE USING
GRAPHITE ELECTRODES

SUMMARY OF THE DOCTORAL DISSERTATION

Major: Mechanical Engineering

Code: 9520103

HANOI, 2026

The dissertation was completed at:

**National Research Institute of Mechanical Engineering –
Ministry of Industry and Trade**

Scientific supervisors:

- 1. Supervisor 1: Prof. Dr. Vu Ngoc Pi**
- 2. Supervisor 2: Assoc. Prof. Dr. Le Thu Quy**

Examiner 1: Assoc. Prof. Dr. Nguyen Huu Phan

Examiner 2: Assoc. Prof. Dr. Bui Ngoc Tuyen

Examiner 3: Assoc. Prof. Dr. Hoang Van Got

**The dissertation was defended before the Institute-level Doctoral
Dissertation Evaluation Committee.**

Venue: National Research Institute of Mechanical Engineering –
Ministry of Industry and Trade

Main building: No. 4 Pham Van Dong Street, Phu Dien Ward, Hanoi,
Vietnam

At hours, on day of month, year.

The dissertation can be consulted at:

1. National Library of Vietnam
2. Library of the National Research Institute of Mechanical Engineering

INTRODUCTION

1. Necessity of the Research

Electrical discharge machining (*EDM*) is widely used for machining hardened materials and complex components due to its high efficiency and low cutting forces. However, it faces limitations such as low material removal rate and trade-offs between surface quality and productivity. Previous studies have analyzed the effects of process parameters on *MRR*, *EWR*, and *Ra*, as well as the influence of electrode vibration and workpiece motion, providing a basis for *EDM* optimization.

To improve *EDM* performance, various approaches have been explored, including parameter optimization, alternative dielectrics, powder-mixed fluids, and vibration assistance. Among these, ultrasonic vibration-assisted *EDM* effectively enhances debris removal and dielectric circulation, improving spark stability, *MRR*, and overall machining performance. Promising results have been reported, especially with graphite electrodes, highlighting the scientific and practical significance of the topic: “Research on machining the external cylindrical surface using electrical discharge machining (*EDM*) with ultrasonic vibration assistance using graphite electrodes.”

2. Research Objectives

The overall objective of the dissertation is to evaluate and improve the machining performance of electrical discharge machining (*EDM*) on the external cylindrical surface of 90CrSi steel, with the aim of achieving high surface quality and optimal productivity through ultrasonic vibration assistance using a graphite HK2 electrode.

3. Research Subject and Scope

The research subject is the ultrasonic vibration-assisted *EDM* process for machining the external cylindrical surface with a graphite HK2 electrode.

The research scope is limited to 90CrSi steel with a diameter of $\text{Ø}14 \pm 0.01$ mm and a graphite HK2 electrode with a diameter of $\text{Ø}12 \pm 0.01$ mm.

The experiments are conducted on a Sodick CNC *EDM* machine (Japan), model Mark A30.

4. Research Methods

The study employs a combination of theoretical analysis and experimental investigation.

5. Research Content

The study includes a literature review, theoretical analysis, selection and design of the ultrasonic horn, and experimental investigation of the effects of key process parameters, including discharge current (I_p), pulse-on time (T_{on}), pulse-off time (T_{off}), discharge voltage (SV), and ultrasonic amplitude (A), on material removal rate (*MRR*), surface roughness (*Ra*), and electrode wear rate (*EWR*) during *EDM* of the external cylindrical surface of 90CrSi steel using a graphite HK2 electrode.

6. Scientific and Practical Significance

* Scientific significance::

This study investigates the influence of ultrasonic vibration on the *EDM*

process and identifies the optimal parameter set and vibration system to improve machining efficiency. The dissertation contributes to the research direction of ultrasonic vibration-assisted *EDM*.

The results of the dissertation can serve as a reference for further scientific research in the field of mechanical machining.

*** Practical significance:**

- The application of ultrasonic vibration to *EDM* of the external cylindrical surface enhances machining performance in practical production, particularly in mold and die manufacturing.

- The research results can serve as reference materials for teaching and research in the field of mechanical machining.

Novel contributions of the dissertation:

- This study is among the pioneering works on ultrasonic vibration-assisted *EDM* (*UV-EDM*) applied to external cylindrical surface machining. The cylindrical geometry presents challenges for conventional *EDM* due to debris accumulation and unstable discharge conditions..

- The use of graphite electrodes, which have good electrical conductivity and are easy to shape but prone to wear, makes them suitable for evaluating the effectiveness of ultrasonic vibration in reducing electrode wear rate (*HWR*).

- The study focuses on both single-objective and multi-objective optimization, including material removal rate, surface roughness, and electrode wear, in line with practical production requirements..

Structure of the dissertation: 4 chapters

CHAPTER 1. OVERVIEW OF ULTRASONIC VIBRATION-ASSISTED ELECTRICAL DISCHARGE MACHINING

1.1 Overview of Electrical Discharge Machining (*EDM*)

1.1.1. Development History

Electrical discharge machining (*EDM*), originating in the 18th century and developed in the mid-20th century, has been significantly improved by advances in pulse generation, wire *EDM*, and numerical control. Currently, hybrid *EDM* methods, especially those assisted by ultrasonic vibration, are promising for enhancing the machining performance of difficult-to-machine and ultra-hard materials.

1.1.2 Principle of Electrical Discharge Machining (*EDM*)

The *EDM* discharge process occurs cyclically in pulse cycles, including:

- Pulse-on time (T_{on}): The duration during which the spark is generated and material is removed.

- Pulse-off time (T_{off}): The interval during which the dielectric recovers and debris is flushed away.

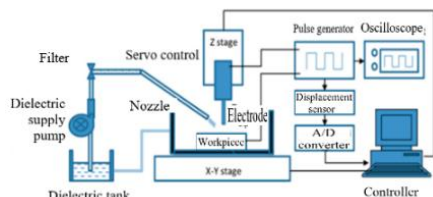


Figure 1.1. Schematic diagram of electrical discharge machining (*EDM*)

- The pulse generator controls the pulsed current supplied to the electrode.
- Servo Control System.
- Dielectric Tank, Pump, and Filtration System.
- Oscilloscope, Displacement Sensor, and A/D Converter.

1.1.3 Basic Process Parameters of Electrical Discharge Machining

Discharge voltage (SV). Pulse current (I_p).

Pulse-on time (T_{on}). Pulse-off time (T_{off}).

1.1.4. Performance Metrics of Electrical Discharge Machining (EDM)

Material removal rate (MRR), electrode wear rate (EWR), surface quality, and machining accuracy.

1.2. Overview of Ultrasonic Vibration-Assisted Electrical Discharge Machining

1.2.1. Necessity of Ultrasonic Vibration in Electrical Discharge Machining

The integration of ultrasonic vibration in EDM enhances debris removal and discharge stability, leading to improved productivity, reduced electrode wear, and better surface quality. Consequently, ultrasonic vibration-assisted EDM shows superior performance for machining difficult-to-machine materials and broadens its applicability in modern manufacturing.

1.2.2. Principle of Ultrasonic Vibration-Assisted Electrical Discharge Machining

Ultrasonic vibration enhances EDM through three main mechanisms: (1) dielectric agitation via cavitation, improving debris removal; (2) periodic modulation of the discharge gap, enhancing circulation and energy distribution; and (3) thermo-mechanical effects that reduce localized heat and surface stresses.

1.2.3 Types of Ultrasonic Vibration Used in Electrical Discharge Machining

Classification based on vibration direction and mode: Axial vibration (ID), torsional vibration (ID torsional), combined longitudinal-torsional vibration (LTV), two-dimensional circular vibration (UCV), and transverse vibration (in the horizontal direction of the workpiece). Classification based on the vibrating component: Electrode vibration, workpiece vibration, and dielectric fluid vibration.

1.3 Overview of Global Research on Ultrasonic Vibration-Assisted Electrical Discharge Machining

Ultrasonic vibration has been studied since early machining developments and integrated into EDM since the mid-20th century. Since the 2000, $UV-EDM$ research has focused on quantifying its effects, consistently showing advantages over conventional EDM . Recently, advanced $UV-EDM$ configurations have been proposed to address challenging machining problems and expand its application potential.

Process Mechanisms and Modeling: In $UV-EDM$, ultrasonic vibration induces local vortices and causes significant fluctuations in the velocity–pressure field within the discharge gap. As a result, the dielectric flow transitions from a laminar to a turbulent regime, thereby significantly altering the hydrodynamic conditions compared with conventional EDM .

1.4 Domestic Research Status

In Vietnam, *EDM* research has primarily focused on optimizing *EDM* and *PMEDM* to improve productivity and surface quality. Studies on mechanical vibration, such as Le Quang Dung et al., show that low-frequency vibration enhances MRR while reducing surface roughness and electrode wear. More recently, V.T. Dinh advanced *UV-EDM* by designing and experimentally validating an ultrasonic horn for external cylindrical machining, opening a promising research direction in Vietnam.

1.5 Overview of Research Trends

Ultrasonic vibration-assisted *EDM* has shown superior performance and expanded application potential. However, its application to machining the external cylindrical surface of 90CrSi steel with graphite electrodes remains limited. Therefore, this study addresses this gap, providing a scientific and practical basis for further application of *UV-EDM*.

Conclusion of Chapter 1:

- *UV-EDM* has been demonstrated to enhance machining performance, surface quality, and process stability in machining difficult-to-machine materials.
- The application of *UV-EDM* to external cylindrical surface machining using graphite electrodes remains limited and requires further experimental investigation.
- Ultrasonic vibration improves the material removal mechanism and surface formation through the dispersion of discharge energy and enhanced cavitation effects.
- These findings provide a basis for selecting process parameters and developing the experimental design in the subsequent chapter.

CHAPTER 2. RESEARCH METHODS AND EXPERIMENTAL SYSTEM

2.1 Box–Behnken Experimental Design Method

The Box–Behnken design (*BBD*) within RSM is used to develop the experimental matrix for modeling and optimizing *Ra*, *MRR*, and *HWR*. Five input parameters are considered: *A* (μm), *T_{on}* (μs), *T_{off}* (μs), *I_p* (A), and *SV* (V). A second-order regression model is then established as follows:

$$y = \beta_0 + \sum_{i=1}^k \beta_i x_i + \sum_{i=1}^k \beta_{ii} x_i^2 + \sum_{i < j} \beta_{ij} x_i x_j + \varepsilon$$

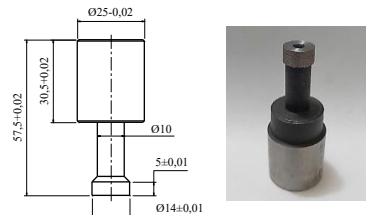
2.2 Research Methods

The study applies a multi-objective optimization framework, including experimental design, data processing using the Box–Cox transformation, modeling based on Gaussian Process Regression (*GPR*), and solving the optimization problem using the *NSGA-II* algorithm, combined with the Analytic Hierarchy Process (*AHP*) to select the optimal solution.

2.3 Experimental System Design

2.3.1 Workpiece Material: 90CrSi Steel

The workpiece is 90CrSi steel, selected based on the dimensions of a tablet-forming punch, as shown in Figure 2.1.



Hình 2.1 Chi tiết gia công 90CrSi

2.3.2 Electrode Material: Graphite HK2

The graphite HK2 electrode has the geometry and dimensions as shown in Figure 2.3.

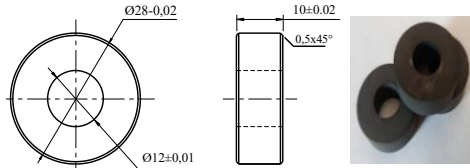


Figure 2.3 Graphite HK2 electrode

2.4 Ultrasonic Horn Design

The optimal design of the ultrasonic horn remains a critical challenge. As it directly affects vibration amplitude, resonance conditions, and fatigue strength, the geometry and dimensions of the *horn* play a decisive role in vibration transmission efficiency.

2.4.1 Basis of Ultrasonic Horn Design

The *horn* is designed to achieve resonance at 20 kHz to obtain the maximum vibration amplitude at the contact surface with the workpiece, corresponding to the antinode of the longitudinal standing wave. This is achieved by optimizing the horn geometry so that the contact position is located at approximately $\lambda/4$ from the vibration node at the transducer–horn interface, thereby amplifying the vibration amplitude and enhancing energy transmission efficiency into the machining zone. The ultrasonic *horn* assembly is shown in Figure 2.4. The ultrasonic generator (1) is mounted on the EDM machine head (2), and the horn (3) is connected to the transducer via a threaded joint. The *horn* is designed with a concentric hole to position and securely clamp the workpiece (4), which is fixed by a nut (5).

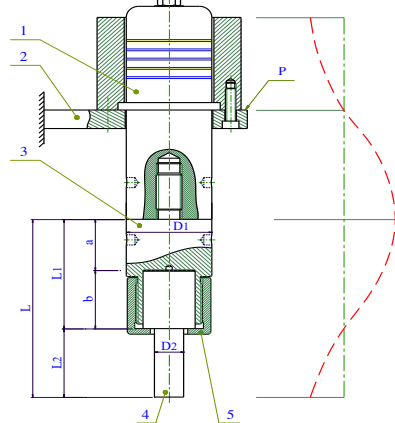


Figure 2.4. Design of the ultrasonic vibration head

- 1. Transducer; 2. EDM machine head;
- 3. Horn; 4. Workpiece; 5. Nut

2.4.2 Theoretical Determination of the Horn Length

For 90CrSi steel, the wave propagation velocity is calculated using the following expression:

$$c = \sqrt{E/\rho} \rightarrow c = \sqrt{205 \cdot 10^9 / 7850} \approx 5110 \text{ m/s}$$

The longitudinal wavelength at the excitation frequency:

$$\lambda = \frac{c}{f} = \frac{5110}{20000} = 255,5 \text{ mm}$$

$$L = \frac{\lambda}{2} = 127,75 \text{ mm}; b = L - a - L_2 = 127,75 - 37 - 27 = 63,75 \text{ mm}$$

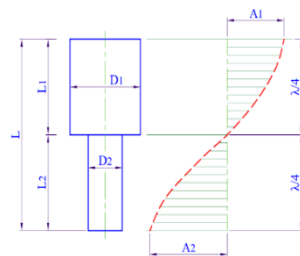


Figure 2.5. Longitudinal vibration mode of the stepped horn

2.4.3 Experimental Determination of the Horn Length

Step 1: Experimental determination of the resonant length corresponding to the maximum vibration amplitude

Based on the theoretical resonance condition, the target length is determined as $L = 127,75$ mm. Four preliminary horn specimens are fabricated with total lengths of 125, 126, 127, and 128 mm, respectively. The length L is obtained by varying the design parameter b from 61 to 64 mm with an increment of 1 mm, while keeping $a = 64$ mm constant in the expression $L = a + b$.

The axial vibration amplitude of each horn is measured using a laser displacement sensor (Keyence LK-H055). The experimental setup is illustrated in Figure 2.7. The measured amplitudes corresponding to different horn lengths are summarized in Table 2.5. In addition, the relationship between horn length and vibration amplitude is presented in Figure 2.8.

Step 2: Adjustment of the horn length to obtain different vibration amplitude levels for the experimental design.

Additional horn configurations are designed to support the Box–Behnken experimental design (BBD) in the optimization stage of UV-EDM. In the BBD matrix, the ultrasonic vibration amplitude (A) is treated as one of the five input variables and defined at three levels to construct a second-order regression model and capture potential nonlinear effects.

Table 2.5. Vibration amplitude of the horn for $b = 61\text{--}64$ mm (step = 1 mm)

b (mm)	L (mm)	A (μm)
64,0	128,0	5,01
63,0	127,0	5,12
62,0	126,0	5,20
61,0	125,0	4,94

The maximum vibration amplitude measured in Step 1 is $5.2 \mu\text{m}$ at a horn length of $L = 126$ mm, which is selected as the high level for variable A . To determine the remaining two levels, $1.2 \mu\text{m}$ and $3.2 \mu\text{m}$, additional horn specimens are fabricated by adjusting the parameter b , i.e., by varying the

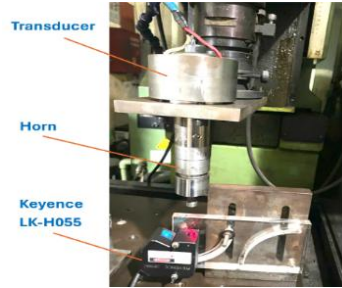


Figure 2.7. Vibration amplitude measurement setup

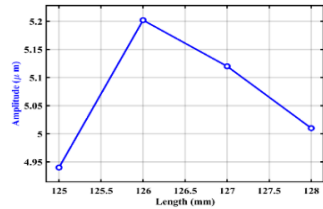


Figure 2.8. Relationship between the total horn length L and vibration amplitude A (coarse step)

Table 2.6. Horn length (L) and vibration amplitude (A) obtained by varying b

b (mm)	L (mm)	A (μm)
11,30	75,30	1,21
30,50	94,50	3,18
62,00	126,00	5,20
93,00	157,00	3,80

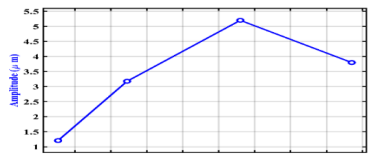


Figure 2.9. Relationship between horn length (L) and vibration amplitude (A)

total length according to $L = a + b$.

The *horn* lengths corresponding to the target amplitude values are presented in Table 2.6. The relationship between *horn* length and vibration amplitude is illustrated in Figure 2.9, revealing a nonlinear trend and a high sensitivity to resonance conditions.

2.5 Experimental Design and Data Collection

2.5.1 Experimental Setup

A CNC EDM machine (Sodick, model Mark A30) is employed. The ultrasonic vibration system consists of an MPI WG-3000 generator with a maximum power of 3000 W, connected to an ultrasonic transducer (RPS-5020-4Z) with a power rating of 2000 W and an operating frequency of 20 kHz. The experimental design includes five input process parameters: A , T_{on} , T_{off} , I_p and SV .



Figure 2.10 UV-EDM experimental setup

2.5.2 Measurement Equipment

Surface roughness Ra (μm): Measured using a Mitutoyo SV-3100 instrument.

Material removal rate (MRR) (g/h): Calculated from the workpiece mass before and after machining, measured using an electronic balance (WT3003NE, resolution 0.001 g). The machining time is recorded directly from the CNC machine control program.

A digital microscope (PS-530G) is used to capture longitudinal cross-sectional images of the electrode after the EDM process, for measuring and analyzing the vertical electrode wear rate (HWR , mm/h).

2.5.3 Experimental Procedure and Data Collection

Five input process parameters investigated in this study are presented in Table 2.7. All input and output data from the 46 experiments are verified and processed prior to being imported into *MATLAB* for regression model development and subsequent optimization. The results of Ra , MRR , and HWR for each combination of process parameters are presented in Table 2.8.

Table 2.7 Input process parameters

TT	Input parameters		Factor levels		
1	Ultrasonic vibration amplitude	A (μm)	1,2	3,2	5,2
2	Pulse-on time	T_{on} (μs)	8	12	16
3	Pulse-off time	T_{off} (μs)	8	12	16
4	Discharge current	I_p (A)	5	10	15
5	Discharge voltage	SV (V)	4	5	6

Table 2.8. Experimental design and results

No.	A (μm)	T_{on} (μs)	T_{off} (μs)	I_p (A)	SV (V)	MRR (g/h)	Ra (μm)	HWR (mm/h)
1	1,2	8	12	10	5	3,527	2,327	1,031
2	1,2	16	12	10	5	5,898	3,806	0,286

3	5,2	8	12	10	5	5,764	3,565	0,947
4	5,2	16	12	10	5	7,437	3,878	0,423
5	3,2	12	8	5	5	4,472	4,046	0,069
6	3,2	12	8	15	5	8,427	5,548	0,593
7	3,2	12	16	5	5	3,844	3,879	0,368
8	3,2	12	16	15	5	7,941	4,627	0,691
9	3,2	8	12	10	4	5,738	2,201	0,890
10	3,2	8	12	10	6	6,019	2,767	1,235
11	3,2	16	12	10	4	9,391	4,835	0,055
12	3,2	16	12	10	6	9,182	3,039	0,452
13	1,2	12	8	10	5	4,351	3,945	0,509
14	1,2	12	16	10	5	3,531	3,070	0,489
15	5,2	12	8	10	5	6,380	3,846	1,026
16	5,2	12	16	10	5	4,933	3,553	0,437
17	3,2	12	12	5	4	3,659	4,201	0,356
18	3,2	12	12	5	6	3,810	3,927	0,250
19	3,2	12	12	15	4	8,024	5,981	0,854
20	3,2	12	12	15	6	8,017	6,189	0,754
21	3,2	8	8	10	5	6,081	1,915	1,553
22	3,2	8	16	10	5	6,323	1,838	1,329
23	3,2	16	8	10	5	9,737	5,153	0,966
24	3,2	16	16	10	5	8,178	4,662	0,065
25	1,2	12	12	5	5	2,582	4,405	0,109
26	1,2	12	12	15	5	5,488	4,815	1,079
27	5,2	12	12	5	5	3,436	4,080	0,189
28	5,2	12	12	15	5	7,274	4,574	0,861
29	3,2	12	8	10	4	9,035	3,174	0,928
30	3,2	12	8	10	6	6,832	3,128	0,432
31	3,2	12	16	10	4	7,255	3,464	0,331
32	3,2	12	16	10	6	7,068	4,003	1,064
33	1,2	12	12	10	4	4,510	4,059	0,415
34	1,2	12	12	10	6	5,475	3,205	0,385
35	5,2	12	12	10	4	4,879	3,091	0,272
36	5,2	12	12	10	6	5,066	3,792	0,251
37	3,2	8	12	5	5	2,703	2,093	0,568
38	3,2	8	12	15	5	5,674	3,461	1,411
39	3,2	16	12	5	5	6,862	1,818	0,163
40	3,2	16	12	15	5	10,239	10,627	0,335
41	3,2	12	12	10	5	6,426	4,098	0,195
42	3,2	12	12	10	5	7,386	3,976	0,699
43	3,2	12	12	10	5	7,481	3,913	0,293
44	3,2	12	12	10	5	7,634	4,020	0,273
45	3,2	12	12	10	5	6,282	3,859	0,222
46	3,2	12	12	10	5	7,717	3,969	0,477

Conclusion of Chapter 2

- An ultrasonic vibration-assisted *EDM (UV-EDM)* configuration is proposed, where vibration is directly transmitted to the workpiece via a horn, improving discharge stability.

- The *horn* is designed and optimized using a combined theoretical–experimental approach, achieving resonance at 126 mm with a vibration amplitude of 5.2 μm for the Box–Behnken design.

- The results provide a basis for evaluating the effects of ultrasonic amplitude on *MRR*, *Ra*, and *HWR*.

- An axial vibration configuration is selected to enhance debris removal and improve process stability in external cylindrical machining.

CHAPTER 3. SINGLE-OBJECTIVE OPTIMIZATION OF *Ra*, *MRR*, AND *HWR*

3.1 Process Modeling Using *RSM* and *GPR*

The response surface methodology (*RSM*) is employed to develop second-order regression models for single-objective optimization. Gaussian Process Regression (*GPR*) is applied to enhance the capability of capturing nonlinear behavior and to improve prediction accuracy when the *RSM* model is insufficient.

3.1.1 Theoretical Basis of *RSM*

The general form of the second-order regression model with k input variables is given as follows: $y = \beta_0 + \sum_{i=1}^k \beta_i x_i + \sum_{i=1}^k \beta_{ii} x_i^2 + \sum_{i < j} \beta_{ij} x_i x_j + \varepsilon$ (3.1)

3.1.2 Analysis of Variance (*ANOVA*) and Model Adequacy

Surface Roughness Model (*Ra*)

Table 3.1 presents the regression coefficients and p-values for the surface roughness model (*Ra*, μm). The second-order regression model for *Ra* has a coefficient of determination $R^2 = 0.7868$ and an adjusted coefficient of determination $R_{\text{adj}}^2 = 0.6163$, indicating that the model explains approximately 78.7% of the variance in the response data. Among the input factors, the discharge current (I_p) has a significant effect on *Ra* ($p = 0.0189$). In addition, the interaction effect between T_{on} and I_p is statistically significant ($p = 0.0003$), indicating a strong relationship between T_{on} and *Ra*.

Table 3.1. Regression coefficients and p-values for the *Ra* model (μm)

Model term	Coefficient	p-value	Model term	Coefficient	p-value
(Intercept)	-4,2282	0,7948	$T_{\text{on}} \times I_p$	0,0930	0,0003
<i>A</i>	0,4510	0,7807	$T_{\text{on}} \times SV$	-0,1476	0,1889
T_{on}	0,9525	0,2576	$T_{\text{off}} \times IP$	-0,0094	0,6702
T_{off}	0,3270	0,6943	$T_{\text{off}} \times SV$	0,0366	0,7406
<i>IP</i>	-1,5898	0,0189	$I_p \times SV$	0,0241	0,7848
<i>SV</i>	2,1176	0,5676	A^2	-0,0778	0,3965
$A \times T_{\text{on}}$	-0,0604	0,2730	T_{on}^2	-0,0260	0,1718
$A \times T_{\text{off}}$	0,0098	0,8571	T_{off}^2	-0,0163	0,3866
$A \times I_p$	-0,0252	0,5645	I_p^2	0,0376	0,0039
$A \times SV$	0,1874	0,3926	SV^2	-0,1604	0,5926
$T_{\text{on}} \times T_{\text{off}}$	-0,0065	0,8151			

Material Removal Rate Model (*MRR*)

The model for *MRR* exhibits excellent performance, with $R^2 = 0.9250$ and an adjusted coefficient of determination $R_{\text{adj}}^2 = 0.8649$ (Table 3.2), indicating that more than 92% of the variation in *MRR* is explained by the model. The factors influencing *MRR* include the ultrasonic amplitude (*A*) ($p = 0.0004$) and the discharge

current (I_p) ($p = 0,0487$). In addition, the quadratic terms of A and I_p are statistically significant ($p < 0,0005$), reflecting strong nonlinear effects of these variables on MRR .

Table 3.2. Regression coefficients and p -values for the MRR model (g/h)

Model term	Coefficient	p-value	Model term	Coefficient	p-value
(Intercept)	-8,1350	0,5389	$T_{on} \times I_p$	0,0051	0,7773
A	5,3330	0,0004	$T_{on} \times SV$	-0,0306	0,7330
T_{on}	0,3793	0,5750	$T_{off} \times I_p$	0,0018	0,9215
T_{off}	-0,3624	0,5921	$T_{off} \times SV$	0,1260	0,1679
I_p	1,0653	0,0487	$I_p \times SV$	-0,0079	0,9122
SV	-0,8404	0,7794	A^2	-0,6437	0,0000
$A \times T_{on}$	-0,0427	0,3385	T_{on}^2	0,0238	0,1260
$A \times T_{off}$	-0,0255	0,5650	T_{off}^2	0,0011	0,9448
$A \times I_p$	0,0167	0,6381	I_p^2	-0,0391	0,0004
$A \times SV$	-0,0367	0,8357	SV^2	-0,0188	0,9382
$T_{on} \times T_{off}$	-0,0281	0,2163			

Vertical Electrode Wear Rate Model (HWR)

Table 3.3. Regression coefficients and p -values for the HWR model (μm)

Model term	Coefficient	p-value	Model term	Coefficient	p-value
(Intercept)	8,5578	0,0479	$T_{on} \times I_p$	-0,0084	0,1466
A	0,1298	0,7541	$T_{on} \times SV$	0,0033	0,9077
T_{on}	-0,3594	0,0999	$T_{off} \times I_p$	-0,0025	0,6562
T_{off}	-0,5212	0,0203	$T_{off} \times SV$	0,0768	0,0110
I_p	0,1681	0,3093	$I_p \times SV$	0,0003	0,9894
SV	-1,4459	0,1346	A^2	0,0103	0,6589
$A \times T_{on}$	0,0094	0,5016	T_{on}^2	0,0179	0,0008
$A \times T_{off}$	-0,0196	0,1665	T_{off}^2	0,0135	0,0087
$A \times I_p$	-0,0030	0,7883	I_p^2	0,0013	0,6743
$A \times SV$	-0,0081	0,8836	SV^2	0,0550	0,4746
$T_{on} \times T_{off}$	-0,0106	0,1425			

Table 3.3 presents the regression coefficients and p -values for the HWR model (mm/h). The HWR model shows a moderate level of fit, with $R^2 = 0,8166$ and an adjusted coefficient of determination $R^2_{\text{adj}} = 0,6699$. The statistically significant factors include the pulse-off time (T_{off}) ($p = 0,0203$) and the interaction between T_{off} and SV ($p = 0,0110$). In addition, the quadratic terms of T_{on} and T_{off} also have significant effects on HWR ($p = 0,0008$ and $p = 0,0087$, respectively), indicating the nonlinear nature of the vertical electrode wear process.

Overall Model Evaluation: The second-order regression models developed for the objective functions R_a , MRR , and HWR are capable of capturing the general trends of the experimental data within the investigated design space. The MRR model demonstrates a high level of fit ($R^2 = 0,9250$; $R^2_{\text{adj}} = 0,8649$), in which the ultrasonic amplitude (A) and discharge current (I_p) exhibit significant nonlinear effects. In contrast, the R_a and HWR models show only moderate agreement, with adjusted coefficients of determination of 0,6163 and 0,6699, respectively.

Therefore, Gaussian Process Regression (*GPR*) is employed in the subsequent sections to improve prediction accuracy and enhance the optimization performance for these two responses.

3.2 Modeling of the Three Objective Functions Using *RSM*

Based on the experimental data obtained from the Box–Behnken design and the results of second-order regression analysis using response surface methodology (*RSM*), mathematical models describing the relationships between the five input process parameters ($A, T_{on}, T_{off}, I_p, SV$) and the three output responses (R_a, MRR , and HWR) have been developed. These models can be used to predict the output responses with high accuracy within the investigated range.

3.2.1 Surface Roughness Model (R_a)

The second-order regression equation for $R_a(\mu\text{m})$ is given as follows:

$$\begin{aligned}
 Ra = & -4.2282 + 0.4510A + 0.9525Ton + 0.3270Toff - 1.5898IP + 2.1176SV \\
 & - 0.0604A \cdot Ton + 0.0098A \cdot Toff - 0.0252A \cdot IP + 0.1874A \cdot SV \\
 & - 0.0065Ton \cdot Toff + 0.0930Ton \cdot IP - 0.1476Ton \cdot SV \\
 & - 0.0094Toff \cdot IP + 0.0366Toff \cdot SV + 0.0241IP \cdot SV \\
 & - 0.0778A^2 - 0.0260Ton^2 - 0.0163Toff^2 + 0.0376IP^2 - 0.1604SV^2
 \end{aligned} \tag{3.2}$$

The model adequacy is evaluated using a comparison plot between predicted and experimental values (Figure 3.4) and a residual plot (Figure 3.5). Figure 3.4 shows that the data points are closely distributed around the 45° diagonal line, indicating a relatively good agreement between the predicted and experimental values. Some deviations are observed in the high- R_a region; however, the overall trend is still consistently captured by the model. The adjusted coefficient of determination $R_{adj}^2 = 0,6163$ confirms that the model explains approximately 61,63% of the variation in R_a , representing a moderate level of fit given the noisy and nonlinear characteristics of the EDM process.

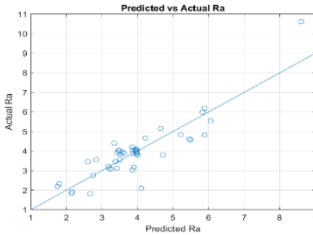


Figure 3.4 Relationship between experimental and predicted values of R_a

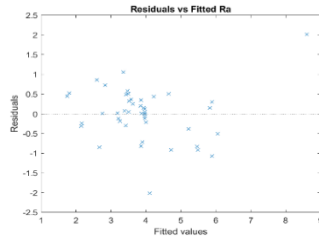


Figure 3.5. Residual plot versus predicted values of R_a

Figure 3.5 further supports this assessment, as the residuals are randomly distributed around the zero axis with no discernible trend or evidence of heteroscedasticity. These observations indicate that the model has acceptable statistical adequacy and moderate reliability for analyzing and predicting R_a within the investigated range.

3.2.2 Material Removal Rate Model (*MRR*)

The second-order regression equation for MRR (g/h) is given as follows:

$$\begin{aligned}
MRR = & -8.1350 + 5.3330A + 0.3793Ton - 0.3624Toff + 1.0653IP - 0.8404SV \\
& - 0.0427A \cdot Ton - 0.0255A \cdot Toff + 0.0167A \cdot IP - 0.0367A \cdot SV \\
& - 0.0281Ton \cdot Toff + 0.0051Ton \cdot IP - 0.0306Ton \cdot SV \\
& + 0.0018Toff \cdot IP + 0.1260Toff \cdot SV - 0.0079IP \cdot SV \\
& - 0.6437A^2 + 0.0238Ton^2 + 0.0011Toff^2 - 0.0391IP^2 - 0.0188SV^2
\end{aligned} \tag{3.3}$$

The adequacy of the model is illustrated by a comparison plot between the predicted and experimental values (Figure 3.6), along with the residual plot (Figure 3.7). The modeling results show that the predicted *MRR* values closely follow the experimental data, as evidenced by the distribution of data points along the diagonal line in the predicted–actual plot.

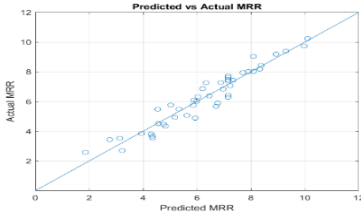


Figure 3.6. Relationship between experimental and predicted values of *MRR*

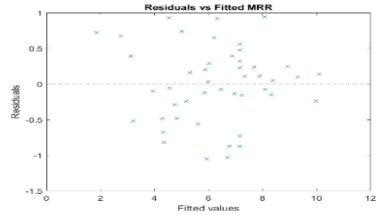


Figure 3.7 Residual plot versus predicted values of *MRR*

The residual plot indicates that the residuals are randomly distributed around zero, with no observable trend or evidence of heteroscedasticity, thereby confirming that the fundamental assumptions of the regression model are satisfied. The values $R^2 = 0,9250$ and $R_{adj}^2 = 0,8649$ demonstrate that the model has strong explanatory power and does not exhibit overfitting.

3.2.3 Regression Model for Vertical Electrode Wear Rate (*HWR*)

The second-order regression equation for *HWR* (mm/h) is given as follows:

$$\begin{aligned}
HWR = & 8.5578 + 0.1298A - 0.3594Ton - 0.5212Toff + 0.1681IP - 1.4459SV \\
& + 0.0094A \cdot Ton - 0.0196A \cdot Toff - 0.0030A \cdot IP - 0.0081A \cdot SV \\
& - 0.0106Ton \cdot Toff - 0.0084Ton \cdot IP + 0.0033Ton \cdot SV \\
& - 0.0025Toff \cdot IP + 0.0768Toff \cdot SV + 0.0003IP \cdot SV \\
& + 0.0103A^2 + 0.0179Ton^2 + 0.0135Toff^2 + 0.0013IP^2 + 0.0550SV^2
\end{aligned} \tag{3.4}$$

The adequacy of the *HWR* model is illustrated in Figures 3.8 and 3.9. The predicted–experimental data points are distributed relatively close to the diagonal line, indicating that the model provides an acceptable level of fit within the investigated domain. The residuals are randomly distributed around zero, with no

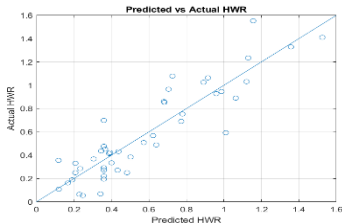


Figure 3.8 Relationship between experimental and predicted values of *HWR*

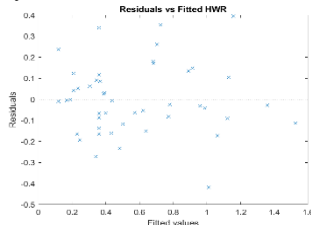


Figure 3.9 Residual plot versus predicted values of *HWR*

observable trend or evidence of heteroscedasticity, thereby satisfying the fundamental assumptions of the regression model. However, with an adjusted coefficient of determination of $R^2_{adj} = 0,6699$, the model explains only about 67% of the variation in *HWR*, which is lower than that of the *MRR* model. This reflects the highly variable and difficult-to-predict nature of *HWR* in the *EDM* process.

3.3 Improving Prediction Models Using Gaussian Process Regression (GPR)

3.3.1 Theoretical Basis

Gaussian Process Regression (*GPR*) is a powerful non-parametric machine learning technique, particularly effective for modeling highly complex nonlinear problems. *GPR* not only provides point predictions but also quantifies prediction uncertainty through probabilistic distributions, which is especially useful when the data are noisy or exhibit unclear nonlinear patterns. In this study, *GPR* is employed as an alternative to *RSM* to predict *Ra* and *HWR*-two response variables for which the previously developed second-order regression models exhibited limited adequacy.

3.3.2 Training of the GPR Model and Selection of the Optimal Kernel Function

The *GPR* models for *MRR*, *Ra*, and *HWR* are developed using multiple kernel functions and implemented in *MATLAB* via the *fitrgp* function, with hyperparameters optimized by maximizing the marginal likelihood. Different configurations are evaluated based on statistical metrics, showing high accuracy, especially with Rational Quadratic and Matérn 3/2 kernels combined with constant or quadratic basis functions. Considering both accuracy and stability, the Rational Quadratic–pure quadratic configuration is selected as the optimal model for *Ra*.

Models employing Matérn 5/2, Matérn 3/2, or Rational Quadratic kernels combined with linear or quadratic basis functions all yield good predictive performance, with R^2 and R^2_{adj} values close to 0,99. Among these, the Matérn 5/2–linear configuration is selected as the optimal model, as it not only achieves high prediction accuracy but also reasonably captures the variation trend of *MRR*.

Models employing Matérn 5/2 or Rational Quadratic kernels combined with

```

=== GPR MRR Comparison (Kernel x Basis) ===
kernel      basis      R^2      R^2adj
squarexponential | constant | 0.9375 | 0.9297
squarexponential | linear   | 0.9881 | 0.9866
squarexponential | pureQuadratic | 0.9881 | 0.9866
rationalQuadratic | constant | 0.9429 | 0.9357
rationalQuadratic | linear   | 0.9881 | 0.9866
rationalQuadratic | pureQuadratic | 0.9881 | 0.9866
matern32     | constant | 0.9881 | 0.9866
matern32     | linear   | 0.9881 | 0.9866
matern32     | pureQuadratic | 0.9881 | 0.9866
matern52     | constant | 0.9873 | 0.9858
matern52     | linear   | 0.9881 | 0.9866
matern52     | pureQuadratic | 0.9881 | 0.9866

```

Figure 3.10 Comparison of GPR model configurations for *Ra*

```

=== GPR Ra Comparison (Kernel x Basis) ===
kernel      basis      R^2      R^2adj
squarexponential | constant | 0.9996 | 0.9996
squarexponential | linear   | 0.9907 | 0.9895
squarexponential | pureQuadratic | 0.5928 | 0.5419
rationalQuadratic | constant | 0.9858 | 0.9840
rationalQuadratic | linear   | 0.9996 | 0.9996
rationalQuadratic | pureQuadratic | 0.9996 | 0.9996
matern32     | constant | 0.9996 | 0.9996
matern32     | linear   | 0.9780 | 0.9753
matern32     | pureQuadratic | 0.9996 | 0.9996
matern52     | constant | 0.9491 | 0.9427
matern52     | linear   | 0.9758 | 0.9739
matern52     | pureQuadratic | 0.5928 | 0.5419

```

Figure 3.11 Comparison of GPR model configurations for *MRR*

```

=== GPR HWR Comparison (Kernel x Basis) ===
kernel      basis      R^2      R^2adj
squarexponential | constant | 0.9726 | 0.9691
squarexponential | linear   | 0.8940 | 0.8807
squarexponential | pureQuadratic | 0.9725 | 0.9691
rationalQuadratic | constant | 0.9726 | 0.9691
rationalQuadratic | linear   | 0.9726 | 0.9691
rationalQuadratic | pureQuadratic | 0.7074 | 0.6708
matern32     | constant | 0.8727 | 0.8568
matern32     | linear   | 0.9686 | 0.9647
matern32     | pureQuadratic | 0.9726 | 0.9691
matern52     | constant | 0.8670 | 0.8504
matern52     | linear   | 0.9726 | 0.9691
matern52     | pureQuadratic | 0.9666 | 0.9624

```

Figure 3.12 Comparison of GPR model configurations for *HWR*

linear basis functions provide the best predictive performance, with R^2 values close to 0,97. The Matérn 5/2–linear configuration is selected as the optimal GPR model for HWR due to its effectiveness in capturing the variation trend of HWR within the investigated domain.

3.3.3 Evaluation of Model Accuracy

a) Evaluation of the GPR Model for Material Removal Rate (MRR)

The data points are closely clustered around the ideal diagonal line, indicating small prediction errors and no evidence of systematic bias across the entire investigated domain. The coefficients of determination are $R^2 = 0,9881$ and $R^2_{adj} = 0,9866$. These values demonstrate that the GPR model accurately captures the nonlinear relationship between the process parameters and MRR.

b) Evaluation of the GPR Model for Surface Roughness (Ra)

The optimal GPR model employs a Rational Quadratic kernel combined with a constant basis function, demonstrating an almost perfect fit to the experimental data. The coefficients of determination are $R^2 = 0,9996$ and $R^2_{adj} = 0,9996$. These values, being close to unity, indicate the excellent modeling capability of the GPR model for Ra .

c) Evaluation of the GPR Model for Vertical Electrode Wear Rate (HWR)

The data points are fairly evenly distributed around the ideal diagonal line, particularly in the low- HWR region, which is of practical importance for finishing operations and extending electrode life. The coefficients of determination are $R^2 = 0,9726$ and $R^2_{adj} = 0,9691$. Although the dispersion of HWR data is higher than that of Ra , the GPR model still demonstrates reliable predictive capability, with small errors and no evidence of systematic bias.

3.3.4 Single-Objective Optimization Using GPR Models

a) Single-objective optimization of Material Removal Rate (MRR)

The optimal GPR model for MRR employs a Matérn 5/2 kernel (*matern52*) combined with a linear basis function, achieving high accuracy with $R^2 = 0,9881$ and $R^2_{adj} = 0,9866$. The optimization results obtained from *MATLAB* indicate that the maximum predicted MRR reaches 10,6379 g/h at the following process

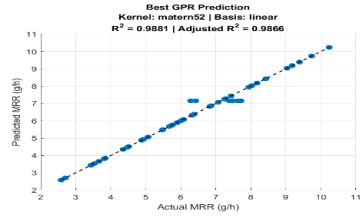


Figure 3.13. GPR model for MRR

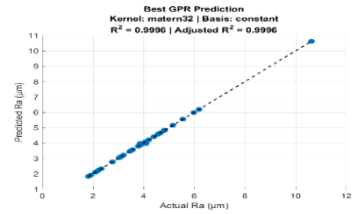


Figure 3.14 GPR model for Ra

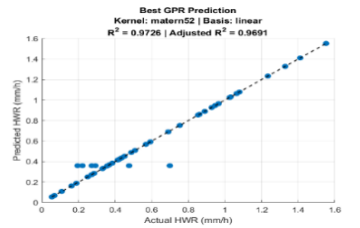


Figure 3.15. GPR model for HWR

parameters: $A = 5,2 \mu\text{m}$, $T_{\text{on}} = 16 \mu\text{s}$, $T_{\text{off}} = 8 \mu\text{s}$, $I_p = 15 \text{ A}$, and $SV = 4 \text{ V}$.

b) Single-objective optimization of Surface Roughness (R_a)

The optimal *GPR* model for R_a employs a Rational Quadratic kernel combined with a constant basis function, yielding an almost perfect fit with $R^2 = 0,9996$ and $R_{\text{adj}}^2 = 0,9996$. The optimization results show that the minimum predicted R_a is $2,0407 \mu\text{m}$ at the following process parameters: $A = 2,938 \mu\text{m}$, $T_{\text{on}} = 8 \mu\text{s}$, $T_{\text{off}} = 12,083 \mu\text{s}$, $I_p = 5,7544 \text{ A}$, and $SV = 4,7723 \text{ V}$.

c) Single-objective optimization of Vertical Electrode Wear Rate (HWR)

The optimal *GPR* model for HWR employs a Matérn 5/2 kernel (*matern52*) combined with a linear basis function, achieving $R^2 = 0,9726$ and $R_{\text{adj}}^2 = 0,9691$. The optimization results indicate that the minimum predicted HWR is 0.0400 mm/h at the following process parameters: $A = 3,1863 \mu\text{m}$, $T_{\text{on}} = 15,8063 \mu\text{s}$, $T_{\text{off}} = 12,7397 \mu\text{s}$, $I_p = 8,0780 \text{ A}$, and $SV = 4,0000 \text{ V}$.

3.3.5 Experimental Validation

- **Optimal parameter set for maximum MRR :** $A = 5,2 \mu\text{m}$, $T_{\text{on}} = 16 \mu\text{s}$, $T_{\text{off}} = 8 \mu\text{s}$, $I_p = 15 \text{ A}$, $SV = 4 \text{ V}$. The experimentally obtained MRR is $10,24 \text{ g/h}$; the relative error compared to the predicted value ($MRR = 10.6379 \text{ g/h}$) is $3,74\%$. This small deviation confirms the reliability of the *GPR* model.

- **Optimal parameter set for minimum surface roughness (R_a):** $A = 2,94 \mu\text{m}$, $T_{\text{on}} = 8 \mu\text{s}$, $T_{\text{off}} = 12 \mu\text{s}$, $I_p = 5,75 \text{ A}$, $SV = 4,8 \text{ V}$.

The experimentally measured R_a is $2.17 \mu\text{m}$; the relative error compared to the predicted value ($R_a = 2,0407 \mu\text{m}$) is $5,96\%$. This deviation is acceptable, confirming the reliability of the *GPR* model.

- **Optimal parameter set for minimum HWR :** $A = 3,1863 \mu\text{m}$; $T_{\text{on}} = 15,8063 \mu\text{s}$; $T_{\text{off}} = 12,7397 \mu\text{s}$; $I_p = 8,078 \text{ A}$; $SV = 4,00 \text{ V}$.

The experimentally obtained HWR is 0.043 mm/h ; the relative error compared to the predicted value ($HWR = 0,0400 \text{ mm/h}$) is $6,97\%$. This deviation remains within an acceptable range, indicating that the *GPR* model provides reliable predictions for HWR .

3.4 Analysis of the Influence of Input Parameters

3.4.1 Basis and Methodology of Analysis

The analysis is conducted using main effect plots (Main Effect Plots), effect bar charts (Effect Bar Plots), and contour plots (Contour Plots). The combined effects of the input parameters on the three responses (R_a , MRR , and HWR) are summarized in Table 3.4.

Table 3.4. Summary of the influence of input parameters on R_a , MRR , and HWR

Parameter	Effect on (R_a)	Effect on MRR	Effect on HWR	Optimization guideline (trade-off)
I_p	↗ Very strong (increases R_a)	↗ Very strong (increases MRR)	↗ Very strong (increases HWR)	Select medium–high levels to increase MRR , while controlling HWR to avoid excessive wear

Parameter	Effect on (R_a)	Effect on MRR	Effect on HWR	Optimization guideline (trade-off)
T_{on}	\nearrow Strong (increases R_a)	\nearrow Strong (increases MRR)	\searrow Strong (reduces HWR)	Select high levels to increase MRR and reduce HWR , but compensate to control R_a
T_{off}	\odot Moderate (nonlinear)	\searrow Slight (MRR not significantly reduced)	$\searrow \downarrow$ Slight (reduces HWR)	Select optimal level (~12 μ s) to balance all three responses
SV	\odot Weak (optimal range exists)	\odot Weak (stable effect)	\nearrow Very slight (increases HWR)	Maintain stable range (4.8–5 V), avoid too low or too high values
A (amplitude)	\searrow Nonlinear (optimal ~3–4 μ m)	\nearrow Nonlinear (increases MRR)	\odot Very slight	Select $A \approx 3\text{--}3.5 \mu\text{m}$ to reduce R_a , increase MRR , and minimally affect HWR

3.5 Single-Objective Optimization of Material Removal Rate (MRR)

3.5.1 Determination of Optimal Parameters Using the RSM Model

The single-objective optimization problem is solved using the *fmincon* function in *MATLAB*, with the objective of maximizing MRR within the experimental constraints: $1,2 \leq A \leq 5,2$; $8 \leq T_{on}$; $T_{off} \leq 16$; $5 \leq I_p \leq 15$ và $4 \leq SV \leq 6$

To facilitate computation, the objective function is multiplied by a negative sign to convert the problem into a minimization of $-MRR$. The optimal solution obtained is: $A = 1,53 \mu\text{m}$; $T_{on} = 16,00 \mu\text{s}$; $T_{off} = 8,00 \mu\text{s}$; $I_p = 15,00 \text{ A}$; $SV = 4,00 \text{ V}$. With this parameter set, the RSM model predicts an MRR of 12,1989 g/h,

3.5.2 Experimental Validation

$A = 1,52 \mu\text{m}$; $T_{on} = 16 \mu\text{s}$; $T_{off} = 8 \mu\text{s}$; $I_p = 15 \text{ A}$; $SV = 4 \text{ V}$.

The workpiece mass before and after machining is measured using an electronic balance to calculate the material removal rate (MRR). The experimentally obtained MRR is 11,572 g/h. Thus, the relative error between the predicted and experimental values is: $(12,1989 - 11,572) * 100 / 11,572 = 5,42 \%$

Conclusion of Chapter 3

- Single-objective modeling and optimization of the *UV-EDM* process for 90CrSi steel were successfully conducted for R_a , MRR , and HWR .
- Discharge current and pulse-on time are the dominant factors, while other parameters mainly ensure process stability.
- Minimizing R_a requires low discharge energy, improving surface quality but reducing MRR ; conversely, maximizing MRR increases R_a and HWR , while HWR can be reduced by limiting thermal impact on the electrode.
- As all objectives cannot be optimized simultaneously, single-objective results provide the basis for multi-objective optimization in Chapter 4.

CHAPTER 4. MULTI-OBJECTIVE OPTIMIZATION

4.1 Introduction

EDM involves inherent trade-offs between MRR and R_a , requiring multi-objective optimization. In *UV-EDM* of 90CrSi steel with graphite electrodes, this

issue is more pronounced. This study therefore aims to maximize MRR while minimizing Ra and HWR to meet both quality and economic requirements.

4.2 Research Methodology

The study adopts a multi-objective optimization framework consisting of the following steps: experimental design; output data preprocessing using the Box–Cox transformation; modeling using Gaussian Process Regression (GPR); solving the multi-objective optimization problem using the $NSGA-II$ algorithm; and selecting optimal solutions using multi-criteria decision-making ($MCDM$) methods.

4.2.1 Experimental Design and Data Collection

(The experimental data are designed and collected as described in Section 2.5.)

4.2.2 Output Data Transformation Using Box–Cox Method

The output responses, including MRR , Ra , and HWR , are transformed using the Box–Cox transformation with the parameter λ varying within the range of -2 to 2 . The optimal value of λ is selected to minimize skewness. Specifically:

- For MRR , the optimal value is $\lambda = 1,00$, indicating that no transformation is required since the original distribution is approximately normal.

- For Ra , the optimal value is $\lambda \approx 1,00$, suggesting the use of a logarithmic transformation: $\log(Ra)$.

- For HWR , the optimal value is $\lambda \approx 0,4$, indicating that a compression transformation is appropriate to reduce positive skewness. The transformed variable is expressed as: $Y^{(0,4)} = \frac{Y^{0,4}-1}{0,4}$ (4.3)

- The distributions before and after transformation are presented in Figures 4.1, 4.2, and 4.3, respectively. The results show that skewness is significantly reduced after transformation, thereby ensuring the validity of subsequent regression modeling, particularly for GPR .

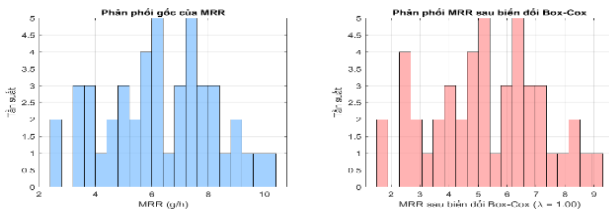


Figure 4.1. Original and Box–Cox transformed distributions of MRR

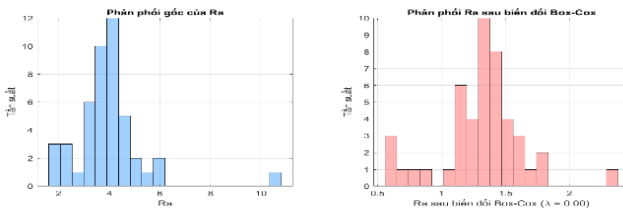


Figure 4.2. Original and Box–Cox transformed distributions of R_a

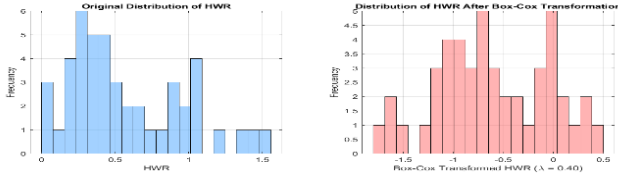


Figure 4.3. Original and Box–Cox transformed distributions of HWR

4.2.3 Regression Modeling Using Gaussian Process Regression (GPR)

The content of this section has been presented in Section 3.3.

4.2.4 Multi-Objective Optimization Using the NSGA-II Algorithm

a) Introduction:

The Non-dominated Sorting Genetic Algorithm II (*NSGA-II*) is employed in this study. *NSGA-II* is a prominent multi-objective evolutionary algorithm known for its ability to maintain population diversity and its high computational efficiency.

b) Objective Functions

The objective function $F(x)$ consists of three components:

$$\text{Maximize } f_1(x) = MRR(x) \quad (4.5)$$

$$\text{Minimize } f_2(x) = Ra(x) \quad (4.6)$$

$$\text{Minimize } f_3(x) = HWR(x) \quad (4.7)$$

where $x = [A, T_{on}, T_{off}, I_p, SV]$ is the vector of design variables.

c) Configuration of the NSGA-II Algorithm

The multi-objective optimization of Ra , MRR , and HWR is performed using *NSGA-II* via the *gamultiobj* function in *MATLAB*. The main settings are as follows:

- Optimization method: *NSGA-II* implemented through *gamultiobj* in *MATLAB*.
- Design variables: Five process parameters: A , T_{on} , T_{off} , I_p , and SV .
- Population and generations: Both set to 200 to ensure solution diversity and stable convergence.
- Genetic operators: Crossover rate of 0.8 and *mutationadaptfeasible* to balance exploration and feasibility.
- Stopping criteria: Termination occurs when the maximum number of generations is reached or when Pareto front improvement falls below 10^{-6} .

4.2.5 Multi-Criteria Decision-Making (MCDM) Methods

Several *MCDM* methods, including *AHP*, *TOPSIS*, *EDAS*, and Entropy weighting, are employed to select the most suitable solution from the Pareto set.

4.3 Optimization Results and Pareto Solution Analysis

4.3.1 Pareto Solutions in the Three-Objective Space

The Pareto solution set in the three-dimensional objective space (MRR – Ra – HWR) is illustrated in Figure 4.4. The existence of trade-offs among the three

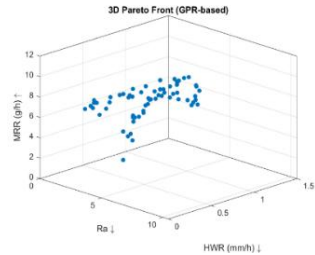


Figure 4.4. 3D Pareto front of MRR , Ra , and HWR obtained using *NSGA-II*

objectives is clearly observed. Solutions with higher MRR values tend to be associated with increased Ra and HWR . Conversely, solutions with lower Ra and HWR generally achieve only moderate MRR levels. The relatively uniform distribution of solutions on the Pareto front indicates that the $NSGA-II$ algorithm, combined with the GPR model, is capable of effectively exploring the solution space, while also revealing the presence of local optima.

4.3.2 Stopping Criteria and Convergence Behavior of the $NSGA-II$ Algorithm

Figure 4.5 illustrates the evolution of four characteristic indicators over generations, including the best MRR value, the minimum Ra , the minimum HWR within the population, and the number of non-dominated solutions.

The MRR value increases rapidly in the early generations, followed by a slower improvement and eventual stabilization, indicating that $NSGA-II$ effectively exploits the search space and achieves good convergence. The minimum values of Ra and HWR decrease significantly at the initial stages and quickly reach a stable state, reflecting the algorithm's strong capability in controlling quality-related objectives.

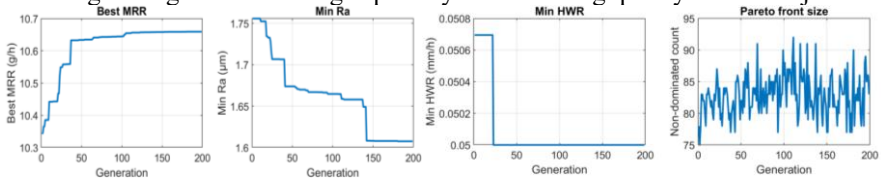


Figure 4.5. Convergence curves of the $NSGA-II$ algorithm
 (a) Best MRR value; (b) Minimum Ra ; (c) Minimum HWR ;
 (d) Number of non-dominated solutions over generations

The number of non-dominated solutions stabilizes after approximately 60 generations, indicating that the structure of the Pareto solution set no longer changes significantly. The $NSGA-II$ algorithm reaches a stable convergence state before termination, ensuring the reliability of the Pareto solution set for subsequent analysis.

4.3.3 Xác định và phân tích điểm *knee* trên Pareto front

From the $MATLAB$ optimization results, the identified knee point corresponds to the following parameter set: $A = 3,086132 \mu\text{m}$, $T_{on} = 15,798762 \mu\text{s}$, $T_{off} = 12,740683 \mu\text{s}$, $I_p = 8,233868 \text{ A}$ and $SV = 4,600083 \text{ V}$. At this point, the predicted responses are $MRR = 8,567433 \text{ g/h}$, $Ra = 3,380038 \mu\text{m}$ and $HWR = 0,148105 \text{ mm/h}$. The knee point lies in the intermediate region, where MRR reaches a relatively high value while Ra and HWR remain at comparatively low levels compared to many other solutions with higher MRR .

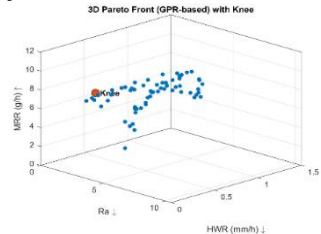


Figure 4.6. 3D Pareto front with the knee point highlighted

The knee point identified in Figure 4.6 represents a solution that achieves a high MRR while maintaining Ra and HWR at well-controlled levels. Therefore, it

serves as a suitable reference for the subsequent decision-making stage using *MCDM* methods.

4.3.4 Trade-off Analysis between Objective Pairs

The trade-off relationships between each pair of objectives are illustrated in Figure 4.7. *MRR–Ra*: As *MRR* increases, *Ra* tends to increase, particularly in the high-*MRR* region, indicating that increasing discharge energy is constrained by the deterioration of surface quality. *MRR–HWR*: A clear trade-off relationship is observed, reflecting increased electrode wear as the discharge energy increases. *Ra–HWR*: These two responses exhibit a similar trend, suggesting that harsh machining conditions simultaneously affect both surface roughness and electrode wear.

4.3.5 Phân tích Pareto theo điểm knee trên các mặt phẳng hai chiều

The *knee* point is highlighted on the two-dimensional Pareto plots in Figure 4.8 to further clarify its role within the objective space. The knee point lies in the intermediate region of all three objectives, where *MRR* attains a relatively high value while *Ra* and *HWR* remain at acceptable levels. This further reinforces the role of the knee point as a representative solution with significant technical and practical relevance.

4.3.6 Pareto Solution Analysis Based on Industrial Requirements

According to industrial requirements, priority is given to maximizing *MRR* while satisfying the constraints $Ra \leq 4 \mu m$ and $HWR \leq 0,6 \text{ mm/h}$, which are considered mandatory technological limits. From the initial Pareto solution set, a subset of feasible solutions that satisfy these constraints is identified. This subset is represented by a highlighted region in the Pareto plots, corresponding to solutions that simultaneously meet surface quality and electrode wear requirements while maintaining relatively high *MRR*. This feasible set serves as the basis for applying multi-criteria decision-making (*MCDM*) methods, including *AHP*, *TOPSIS*, *EAMR*, and *EDAS*, in subsequent steps to select the most suitable machining conditions for practical applications.

4.3.7 General Discussion

Based on the results presented in Figures 4.6 to 4.8, it can be confirmed that the *NSGA-II* algorithm successfully constructs a high-quality Pareto solution set for the multi-objective optimization of the *EDM* process with ultrasonic vibration assistance. The analysis of the Pareto solution set not only clarifies the inherent trade-offs among *MRR*, *Ra*, and *HWR* but also provides a scientific foundation for defining the feasible solution region for subsequent multi-criteria decision-making.

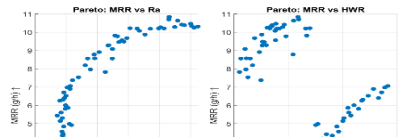


Figure 4.7. Two-dimensional Pareto plots for objective pairs: (a) *MRR–Ra*; (b) *MRR–HWR*; (c) *Ra–HWR*

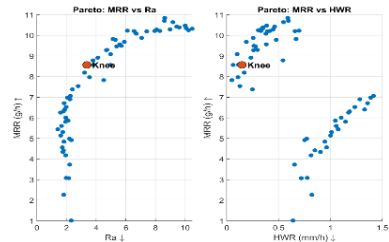


Figure 4.8. Two-dimensional Pareto plots with the knee point highlighted

4.4 Selection of Optimal Solutions from the Pareto Set

To facilitate practical implementation in manufacturing, an optimal representative solution must be selected from the Pareto set. Therefore, a two-step decision-making strategy is adopted: (i) identifying the subset of solutions that satisfy industrial constraints; and (ii) selecting the optimal solution from the feasible subset using multi-criteria decision-making (*MCDM*) methods.

4.4.1 Identification of Feasible Solutions

According to industrial requirements, the following constraints must be satisfied: $Ra \leq 4 \mu\text{m}$ and $HWR \leq 0,6 \text{ mm/h}$

4.4.2 Selection of Optimal Solution Using AHP

Based on the *AHP* results obtained from *MATLAB*, the solution with the highest overall score is identified as the optimal solution. The corresponding parameters are: $A = 3,079858$, $Ton = 15,866091 \mu\text{s}$, $Toff = 12,925115 \mu\text{s}$, $Ip = 10,972303 \text{ A}$ and $SV = 4,681756 \text{ V}$. The predicted responses are $MRR = 9.683182 \text{ g/h}$, $Ra = 5,988281 \mu\text{m}$, and $HWR = 0.189407 \text{ mm/h}$. The *AHP* score of 0.794196 indicates that this solution achieves the highest overall ranking among the Pareto solutions, primarily due to its superior *MRR* performance, despite some trade-off in surface quality. In this study, the *AHP*-selected solution reflects a preference toward maximizing machining productivity, whereas other *MCDM* methods (*TOPSIS*, *EAMR*, and *EDAS*) may yield alternative solutions depending on the weighting of criteria.

4.4.3 Selection of Optimal Solution Using TOPSIS

The *TOPSIS* results include the normalized values k_{ij} , the weight matrix w_j , the separation distances S_i^+ and S_i^- , the closeness coefficient R_i , and the ranking (Table 4.1). Trial 55 achieves the highest R_i value (Rank = 1) and simultaneously belongs to the feasible solution set. This solution corresponds to the following process parameters: $A = 2,896749 \mu\text{m}$, $T_{on} = 15,473460 \mu\text{s}$, $T_{off} = 13,206010 \mu\text{s}$, $I_p = 7,022704 \text{ A}$, and $SV = 4,662458 \text{ V}$. The predicted responses are $MRR = 7,538904 \text{ g/h}$, $Ra = 2,788294 \mu\text{m}$, and $HWR = 0,127529 \text{ mm/h}$. This result indicates that the solution selected by *TOPSIS* not only achieves a high ranking in the mathematical evaluation but also fully satisfies the industrial requirements.

Table 4.1. *TOPSIS*-based evaluation and ranking of Pareto solutions

Trial.	k_{ij}			l_{ij}			S_i^+	S_i^-	R_i	Rank
	Ra	EWR	MRR	Ra	EWR	MRR				
1	0,0316	0,1760	0,0811	0,0086	0,0840	0,0203	0,0826	0,0630	0,4329	58
2	0,1002	0,0082	0,1167	0,0273	0,0039	0,0292	0,0218	0,1154	0,8409	7
3	0,2271	0,0500	0,1528	0,0618	0,0239	0,0383	0,0569	0,0933	0,6211	29
4	0,0851	0,0186	0,1278	0,0232	0,0089	0,0320	0,0176	0,1129	0,8652	4
10	0,0516	0,1047	0,0152	0,0140	0,0500	0,0038	0,0591	0,0781	0,5690	37
11	0,0435	0,1807	0,0896	0,0119	0,0862	0,0224	0,0844	0,0599	0,4151	61
12	0,1646	0,0641	0,1520	0,0448	0,0306	0,0381	0,0451	0,0889	0,6637	22
29	0,1266	0,0430	0,1415	0,0345	0,0205	0,0354	0,0312	0,0997	0,7618	16

30	0,0790	0,0179	0,1188	0,0215	0,0085	0,0298	0,0174	0,1133	0,8667	3
31	0,0751	0,0243	0,1277	0,0204	0,0116	0,0320	0,0165	0,1115	0,8712	2
54	0,1792	0,0731	0,1533	0,0488	0,0349	0,0384	0,0508	0,0844	0,6243	26
55	0,0619	0,0209	0,1124	0,0169	0,0100	0,0282	0,0160	0,1134	0,8760	1
56	0,0716	0,0277	0,1222	0,0195	0,0132	0,0306	0,0174	0,1100	0,8633	5
68	0,0516	0,1047	0,0152	0,0140	0,0499	0,0038	0,0591	0,0781	0,5691	36
69	0,2132	0,0572	0,1549	0,0580	0,0273	0,0388	0,0547	0,0904	0,6231	28
70	0,1042	0,0426	0,1384	0,0284	0,0203	0,0347	0,0264	0,1016	0,7940	12

4.4.4 Selection of Optimal Solution Using *EAMR*

Trial 55 continues to achieve the highest S_i value (Rank = 1) (Table 4.2). This solution coincides with the optimal solution selected by TOPSIS in terms of both process parameters and the corresponding output values (*MRR*, *Ra*, and *HWR*). This consistency indicates the stability and high reliability of Trial 55 when evaluated using different *MCDM* methods.

Table 4.2. *EAMR*-based evaluation and ranking of Pareto solutions

Trial.	n_{ij}			V_{ij}			G_i^-	G_i^+	S_i	Rank
	<i>Ra</i>	<i>EWR</i>	<i>MRR</i>	<i>Ra</i>	<i>EWR</i>	<i>MRR</i>				
1	0,1357	0,7597	0,5019	0,0369	0,3625	0,1258	0,3995	0,1258	0,3149	52
2	0,4310	0,0353	0,7218	0,1173	0,0169	0,1809	0,1342	0,1809	1,3475	6
3	0,9766	0,2159	0,9453	0,2659	0,1030	0,2369	0,3689	0,2369	0,6421	29
4	0,3661	0,0803	0,7906	0,0997	0,0383	0,1981	0,1380	0,1981	1,4358	3
10	0,2217	0,4520	0,0938	0,0604	0,2157	0,0235	0,2760	0,0235	0,0851	70
11	0,1873	0,7803	0,5539	0,0510	0,3723	0,1388	0,4233	0,1388	0,3279	45
12	0,7079	0,2768	0,9401	0,1927	0,1321	0,2356	0,3248	0,2356	0,7253	21
29	0,5446	0,1857	0,8751	0,1483	0,0886	0,2193	0,2369	0,2193	0,9258	16
30	0,3396	0,0771	0,7350	0,0925	0,0368	0,1842	0,1293	0,1842	1,4247	4
31	0,3229	0,1047	0,7900	0,0879	0,0500	0,1980	0,1379	0,1980	1,4360	2
54	0,7707	0,3157	0,9481	0,2098	0,1506	0,2376	0,3605	0,2376	0,6590	26
55	0,2663	0,0902	0,6952	0,0725	0,0430	0,1742	0,1155	0,1742	1,5078	1
56	0,3078	0,1197	0,7557	0,0838	0,0571	0,1893	0,1409	0,1893	1,3435	7
68	0,2218	0,4518	0,0938	0,0604	0,2156	0,0235	0,2760	0,0235	0,0852	69
69	0,9166	0,2470	0,9580	0,2496	0,1179	0,2401	0,3674	0,2401	0,6534	28
70	0,4482	0,1838	0,8561	0,1220	0,0877	0,2145	0,2097	0,2145	1,0230	13

4.4.5 Selection of Optimal Solution Using *EDAS*

Table 4.3 shows that Trial 55 continues to be identified as the optimal solution with the highest AS_i value (Rank = 1). This solution not only belongs to the feasible solution set but also achieves an advantageous position relative to the average values of the entire Pareto solution set, reflecting a good balance and high stability of the proposed machining conditions.

Table 4.3. EDAS-based evaluation and ranking of Pareto solutions

Trial.	SPi'			NSPi	NSNi	ASi	Rank
	Ra	IWR	MRR				
1	0,1871	0,0000	0,0000	0,3863	0,3313	0,3588	58
2	0,0017	0,4388	0,0088	0,9276	1,0000	0,9638	6
3	0,0000	0,2425	0,0891	0,6849	0,4555	0,5702	26
4	0,0424	0,3900	0,0335	0,9621	1,0000	0,9810	4
10	0,1330	0,0000	0,0000	0,2747	0,6313	0,4530	43
11	0,1547	0,0000	0,0000	0,3195	0,3254	0,3224	61
12	0,0000	0,1764	0,0872	0,5445	0,7250	0,6347	23
29	0,0000	0,2754	0,0639	0,7006	0,8888	0,7947	16
30	0,0591	0,3933	0,0135	0,9622	1,0000	0,9811	3
31	0,0696	0,3634	0,0333	0,9629	1,0000	0,9814	2
54	0,0000	0,1341	0,0901	0,4630	0,6620	0,5625	29
55	0,1051	0,3792	0,0000	1,0000	0,9988	0,9994	1
56	0,0790	0,3470	0,0210	0,9232	1,0000	0,9616	7
68	0,1330	0,0000	0,0000	0,2746	0,6315	0,4531	42
69	0,0000	0,2088	0,0937	0,6246	0,5157	0,5701	28
70	0,0000	0,2775	0,0571	0,6908	0,9855	0,8382	13

Overall Discussion:

The results presented in Tables 4.1 to 4.3 indicate that the *TOPSIS*, *EAMR*, and *EDAS* methods consistently identify Trial 55 as the optimal solution within the feasible Pareto solution set.

4.4.6 Selection of Solution Based on Maximum *MRR* within the Feasible Set

The solution corresponding to the maximum *MRR* within the feasible solution set is associated with the following process parameters:

$A = 3,068 \mu\text{m}$, $T_{\text{on}} = 15,613 \mu\text{s}$, $T_{\text{off}} = 9,831 \mu\text{s}$, $I_p = 8,333 \text{ A}$, and $SV = 4,689 \text{ V}$. The predicted responses are $MRR = 8,786 \text{ g/h}$, $Ra = 3,794 \mu\text{m}$, and $HWR = 0,542 \text{ mm/h}$. This solution satisfies the industrial constraints while achieving the highest machining productivity among the acceptable solutions.

4.4.7 Comparison of Optimal Solutions and Final Selection

Table 4.4. Comparison between the knee-point solution and optimal solutions selected by *AHP* and *MCDM* methods

Method	<i>A</i>	T_{on}	T_{off}	<i>IP</i>	<i>SV</i>	<i>MRR</i>	<i>Ra</i>	<i>HWR</i>	Khả thi
<i>knee</i>	3,086	15,799	12,741	8,234	4,600	8,567	3,380	0,148	✓
<i>AHP</i>	3,080	15,866	12,925	10,972	4,682	9,683	5,898	0,189	×
<i>TOPSIS</i>	2,897	15,473	13,206	7,023	4,662	7,539	2,788	0,128	✓
<i>EAMR</i>	2,897	15,473	13,206	7,023	4,662	7,539	2,788	0,128	✓
<i>EDAS</i>	2,897	15,473	13,206	7,023	4,662	7,539	2,788	0,128	✓
<i>MRR max</i>	3,068	15,613	9,831	8,333	4,689	8,786	3,794	0,542	✓

AHP reflects the trend of maximizing *MRR* but does not ensure feasibility,

while the knee point highlights key trade-offs in the *Pareto* set. *TOPSIS*, *EAMR*, and *EDAS* yield stable, feasible solutions. The “maximum *MRR* within the feasible set” is recommended for practical use, balancing productivity with acceptable quality.

Conclusion of Chapter 4

- The *UV-EDM* multi-objective optimization is effectively addressed using *GPR*, *NSGA-II*, and *MCDM*, yielding a well-distributed *Pareto* set and a knee point that supports optimal decision-making.

- *AHP* favors productivity but may degrade surface quality, while *TOPSIS*, *EAMR*, and *EDAS* provide stable, feasible solutions. The “maximum *MRR* within the feasible set” is recommended as a practical option under *Ra* and *HWR* constraints.

- No single solution is universally optimal; selection depends on application goals. The proposed approach is effective and adaptable to other machining optimization problems.

GENERAL CONCLUSIONS AND FUTURE RESEARCH DIRECTIONS

GENERAL CONCLUSIONS

- This dissertation investigates the *UV-EDM* process for machining the external cylindrical surface of 90CrSi steel using graphite HK2 electrodes, based on a Box–Behnken design with five input parameters and three responses (*MRR*, *Ra*, and *HWR*). A reliable *UV-EDM* system integrated with ultrasonic vibration was successfully developed.

- Predictive models were established using regression methods, particularly *GPR*, which provides high accuracy and effectively captures the nonlinear behavior of the process for optimization purposes.

- Single-objective optimization clarified the technological limits and trade-offs among productivity, surface quality, and electrode wear. A hybrid *NSGA-II–GPR* approach was applied for multi-objective optimization, yielding a well-distributed *Pareto* solution set.

- Multi-criteria decision-making (*MCDM*) methods were employed to select optimal solutions, and the “maximum *MRR* within the feasible set” strategy under constraints on *Ra* and *HWR* is recommended for practical applications. The proposed framework demonstrates strong potential for extension to *UV-EDM* and other advanced machining processes.

FUTURE RESEARCH DIRECTIONS

Extend the proposed modeling–optimization framework to difficult-to-machine materials and various dielectric and electrode conditions to assess its generalizability.

Investigate the influence of different ultrasonic vibration transmission modes on machining performance.

Integrate multi-physics models (thermal, electrical, plasma, and fluid flow) to better understand material removal mechanisms, and develop an interactive tool for selecting process parameters based on production priorities.

LIST OF PUBLICATIONS RELATED TO THE DISSERTATION

1. Dinh, V.-T.; Le, T.-Q.; Vu, D.-B.; Vu, N.-P.; **Mai, T.-L***: “*Ultrasonic EDM for External Cylindrical Surface Machining with GGraphite Electrodes: Horn Design and Hybrid NSGA-II–AHP Optimization of MRR and Ra.*” *Machines* 2025, 13, 675. <https://doi.org/10.3390/machines13080675>.
2. Thu-Quy Le; Van-Thanh Dinh; Ngoc-Pi Vu; **Tat-Loi Mai***: “*Analysis and Optimization of Electrode Wear Rate in EDM Using GGraphite Electrodes: A Statistical and GPR-Based Approach*”. *WSEAS Transactions on Applied and Theoretical Mechanics* (accepted, in press),
3. Huu Danh Tran; Hoang Anh Le; Cong Danh Nguyen; Van Thanh; **Tat Loi Mai**; Manh Cuong Nguyen*: “*A Decision-Supporting Multi-Objective Approach for Vibration-Assisted EDM of HARDOX 500 Using NSGA-II and AHP*”. *Engineering, Technology & Applied Science Research* (accepted, in press).
4. Tran Huu Danh, **Mai Tat Loi**², Vu Ngoc Pi and Nguyen Manh Cuong*: “*Multi-objective optimization and decision-making in ultrasonic vibration-assisted EDM of HARDOX 500 using NSGA-II coupled with saw, MARCOS, and TOPSIS*”. *Tạp chí Cơ khí Việt Nam*, số 335, tháng 11/2025.
5. Trần Hữu Danh, Nguyễn Công Danh, **Mai Tất Lợi**, and Nguyễn Mạnh Cường*: “*Simultaneous optimization of material removal Rate and surface roughness in ultrasonic vibration-assisted EDM of HARDOX 500 using NSGA-II and MABAC*”. *Tạp chí Cơ khí Việt Nam*, số 333, tháng 10/2025.